

Characterization of dissimilar aluminum-copper material joining by controlled dual laser beam

Joon Ho Cha

Keimyung University

Hae Woon Choi (✉ hwchoi@kmu.ac.kr)

Keimyung University <https://orcid.org/0000-0001-8063-7586>

Research Article

Keywords: laser welding, battery welding, dual beam, dissimilar material, aluminum copper welding

Posted Date: October 18th, 2021

DOI: <https://doi.org/10.21203/rs.3.rs-980159/v1>

License:   This work is licensed under a Creative Commons Attribution 4.0 International License.

[Read Full License](#)

Version of Record: A version of this preprint was published at The International Journal of Advanced Manufacturing Technology on December 1st, 2021. See the published version at <https://doi.org/10.1007/s00170-021-08324-4>.

Abstract

Laser technology has many advantages in welding for the manufacture of EV battery packs. Aluminum (Al) and copper (Cu) are welded using a dual laser beam, suggesting the optimum power distribution for the core and ring beams. Due to the very high reflectance of Cu and Al exposed to near-infrared lasers, the material absorbs a very small amount of energy. Compared to single beam laser welding, dual beam welding has significantly improved surface quality by controlling surface solidification. The study focused on the quality of weld surface beads, weld properties and tensile strength by varying the output ratio of the core beam to the ring beam. Optimal conditions of Al6061 were a 700 W core beam, a 500 W ring beam and 200 mm/s of weld speed. For the C1020P, the optimum conditions were a center beam of 2500 W, a ring beam of 3000 W and a welding speed of 200 mm/s. In laser lap welding of Al-Al and Al-Cu, the bead width and the interfacial bead width of the joint increased as the output increased. The penetration depth did not change significantly, but small pores were formed at the interface of the junction. Tensile tests were performed to demonstrate the reliability of the weld zone, and computer simulations provided analysis of the heat distribution for optimal heat input conditions.

1. Introduction

As eco-friendly transportation becomes more important, safety and environmental regulations mandate that all means of transport must be lightweight and highly efficient. In the automobile sector, conventional internal combustion engines are being rapidly replaced by eco-friendly electric and hydrogen engines. Electric vehicles (EVs), hybrid electric vehicles (HEVs), and plug-in hybrid vehicles (PHEVs) require a great deal of power; all feature battery packs composed of hundreds to thousands of cells. Unlike the small batteries of mobile and information technology devices, batteries for vehicles must have high-level capacities and be very reliable, so the production requirements are very high.

Recently, the need to co-weld dissimilar materials has increased; this can reduce the weight of automobiles and enable fabrication of high-performance, high-quality battery packs. The principal materials used for EV battery pack fabrication are aluminum (Al) and copper (Cu), exploiting the light weight of Al and the high electrical conductivity of Cu. At the cell level, bonding must be very reliable during hermetic welding of tabs and electrodes and cell container cases. At the module level, tab-to-tab and tab-to-busbar connections are required. At the pack level, an excellent joining technique is required to meet the electrical and structural requirements. All of these electrodes, tabs, busbars, and terminals are fabricated from materials that are difficult to weld, including Cu and Al alloys.

Current battery-welding techniques include resistance spot-welding, laser and ultrasonic welding. It is difficult to co-weld dissimilar high-conductivity materials, and laser welding can address this need. When working with Cu and Al, the formation of brittle intermetallic phases (IMPs) compromises battery performance [1]. Laser welding can yield high quality, precision, and productivity with low deformation. Laser welding can be robotized or otherwise automated or mechanized.

Laser technologies have found many applications in macro-manufacturing welding, cutting, and marking and have greatly improved the competitiveness of the automobile, shipbuilding, and aviation industries. In terms of microelectronics, laser technologies have improved the productivities and add-on values of semiconductors, displays, and multilayer electronic boards, by making it possible to employ novel composite materials. In short, laser processing is a core technology essential for mass production of high-quality devices because lasers facilitate high-speed precise welding and processing[2, 3].

The reflectance of Cu and Al exposed to a near-infrared laser is very high, so the materials absorb very small amounts of energy. Efforts have been made to reduce the thermal effects by creating keyholes in the materials or by using pulsed beams to increase energy absorption) [1–3, 20–21]. Other means of enhancing absorption include laser wobbling or oscillation; in some cases, bonding has employed a brazing technique [1–6, 12]. Recently, green lasers, the energies of which are well-absorbed by Cu, have been developed. Both heat conduction and keyhole welding are possible, because the laser energy absorption of Cu is about 40% at room temperature [5–6, 20]. Also, welding quality is not affected by the nature of the Cu surface (electropolished, sanded, or a simple plate), and is thus highly reproducible. Such welding finds many applications in battery fabrication.

Laser welding of Al and Cu alloys is difficult because both materials have low melting points, high thermal conductivities, and low-level beam energy absorptions [8–11, 13]. The recently developed a dual beam laser operates at a single wavelength (1070 nm), but it is possible to separately control the core and ring beams of a single optical fiber. Compared to single-beam laser welding, dual-beam welding significantly improves surface quality because surface solidification can be controlled [13–15, 18]. When multiple beams are used, keyhole formation can be more stable and spatter can be reduced [15–17].

Here, we explore welding of dissimilar materials using a fiber laser that simultaneously outputs core and ring beams. We focused on welding surface bead quality, welding characteristics, and tensile strength, and varied the output ratios of the core and ring beams. In this research we also analyzed heat distributions via computer simulation. Specifically, we evaluated welding characteristics in terms of the surface qualities and shapes of Al-Cu welds, and used simulations to analyze the heat distributions when heat inputs are controlled during welding. Cross-sections of the laser welds were evaluated in terms of process parameters, and welding reliability was verified by measuring the mechanical properties of welds and by noting any defects.

2. Experimental Setup And Method

2.1 Experimental setup

The fiber laser welding system featured (independently controllable) core and ring beams output by a dual-core optical fiber. Table 1 lists the specifications of laser system and Figure 1 presents the experimental setup and the schematics of beam splits. To optimize laser heat input, the two beams were individually controlled and Figure 2 presents welding specimens and a schematic of the beam delivery system.

Table 1 Specification of laser system

Laser type	FL8000 - ARM (Fiber laser), Coherent Inc.
Wavelength	1.07 μ m
Max. power	Center : 4kW, Ring : 4kW
Beam modulation	Max. 5 kHz
Optical fiber dia.	Center: 70 μ m, Ring : 180 μ m
Scanner	300 x 200mm ,Fd : 560mm

Independent control of the core and ring beams allowed welding to proceed in three stages: pre-heating, keyhole formation, and post-heating. During pre-heating, the surface is heated to below the melting point to increase laser energy absorption; this assists melting stability by removing foreign substances. During keyhole formation, a keyhole and a molten pool are formed by the ring and core beams respectively which yield a deep, narrow weld bead. Finally, post-heating shortens the length of the keyhole and reduces the molten pool; ultimately, both disappear, with maintained weld stability.

We used 0.4 mm thick sheets of the Al (Al6061) and Cu (C1020P) alloys typically employed to fabricate EV battery packs. The Al-Si-Mg-based alloy contained about 0.4 to 0.8% silicon (Si) and about 0.8 to 1.2% magnesium (Mg). We employed an oxygen-free copper C1020P-1/2H alloy. Table 2 lists detailed chemical compositions. The sheets were cut 50 mm in width and the Al plate was placed on top and the Cu for the welding. The materials were overlapped by 45 mm, and 40 mm sections were welded across the width.

Table 2 Chemical composition of Al, Cu alloy (wt. %)

Mat'l	Cu	Si	Mg	Zn	Mn	Cr	Fe	Ti	Al
Al6061	0.4	0.8	< 1.2	< 0.25	< 0.10	< 0.35	< 0.70	< 0.15	Bal.
C1020P		Cu			O ₂				
		> 99.56			< 10 ppm				

To investigate welding characteristics, bead-on-plate (BOP) tests were performed for both Al and Cu. To determine the laser outputs required for the full penetration of the materials, the output was varied with the welding speed and the focal position was held constant.

2.2 BOP and lap joint welding conditions

Because the properties of the two materials differed, it was necessary to optimize welding [19]. The initial welding conditions were established by fixing the focal position and welding speed and then varying the laser output. In general, partial penetration welding is required when welding the tabs and busbars of lithium-ion batteries. Given the high reflectivity of Al and Cu alloys, the laser beam was inclined by 8° with respect to the direction of travel, to ensure that the reflected beam did not attain the laser. Lap joint welding was performed in the manner described above, using specimens with dimensions of 100 x 50 x 0.4 mm. The Al specimens were on top and the Cu specimens on the bottom. Welding was performed over a length of about 40 mm. The laser light source was remotely irradiated (using a galvanometer scanner) without a shielding gas supply.

2.3 Computer simulation

To explore the heat distributions when welding Al and Cu, computer simulations were performed with reference to the experimental conditions. Such simulations effectively track weld heat distribution and deformation based on the temperature distribution [8]. When welding dissimilar materials, the optimal heat input can be predicted by simulation to explore how intermetallic compounds (IMCs) with various physical properties affect weld strength and soundness. During typical welding process, keyholes are generated, and heat thus moves not only via conduction but also via convection. We used the heat transfer module of COMSOL Multiphysics (ver. 5.3a) for numerical analysis. The simulations were verified by comparing the simulated and actual temperature distributions (the latter were assessed using a thermocouple and an infrared camera).

In the simulations, the Al and Cu plates were of the same thicknesses as those of the experiments; the simulation domain was 40 mm in width and 100 mm in length to allow adequate thermal diffusion. The governing three-dimensional heat transfer equation for the entire domain can be expressed as Eq. (1), and the natural convection conditions as Eq. (2):

$$\rho C_p \left(\frac{\partial T}{\partial t} + \mathbf{u}_{trans} \cdot \nabla T \right) + \nabla \cdot (\mathbf{q} + \mathbf{q}_r) = -\alpha T: \frac{dS}{dt} + Q \quad (1)$$

$$\mathbf{q} = -k\nabla T \text{ or } h(T_{ext} - T) \quad (2)$$

where Eq. (2) deals with conductive or convective heat transfer through surrounding bodies. In Eq. (2), ρ is the density of the polymer, C_p is the specific heat capacity at constant stress, T is the absolute temperature, \mathbf{u}_{trans} is the velocity vector of translational motion, k is the thermal conductivity, and q is the heat flux of conduction, q_r is the heat flux of radiation, α is the coefficient of thermal expansion, S is the second Piola-Kirchhoff stress tensor, and Q contains the additional laser heat sources of Eq. (3) or (4).

To simulate the core beam, a three-dimensional (3D) Gaussian laser beam was used, as expressed in Eq. (3). The ring beam can be expressed as Eq. (4). The outer and inner diameters of the ring beam were

established using the Dirac delta function and the “rectangle function” of COMSOL. Figure 3 presents the 3D models of laser beam intensity distributions for each case.

$$Q(x, y, z) = Q_0(1 - R_c) \frac{A_c}{\pi\sigma_x\sigma_y} e^{-\left[\frac{(x-x_0)^2}{\sigma_x^2} + \frac{(y-y_0)^2}{\sigma_y^2}\right]} e^{-[A_c z]} \quad (3)$$

$$\lim_{\varepsilon \rightarrow 0} \int_{x_0-\varepsilon}^{x_0+\varepsilon} \delta(x - x_0) dx = 1 \quad (4)$$

In Eq. (3), Q_0 is the peak power, R_c is the reflectance, σ_x and σ_y are the beam waists in the x and y directions, and A_c is the skin depth/absorption layer thickness. As shown in Eq. (3), the irradiating laser beam was assumed to have a two-dimensional ellipsoidal distribution and a skin depth of A_c in the z direction.

Skin depth can be analytically calculated for any metal. The reflectance (R_c) is important, and was experimentally determined by integrating the sphere. To track the temperature distribution, a temperature probe was placed 0.5 mm distant from the weld line, and then moved to the upper, middle, and lower surfaces in the direction of thickness.

2.4 Weld tests

To test weld strengths, we performed cross-sectional analyses and mechanical strength tests to assess surface cracks and voids. For weld analysis, the specimens were cut, polished, etched, and observed under a microscope. The Al etching solution was hydrochloric acid 75 mL + nitric acid 25 mL; the Cu etching solution was nitric acid 30 mL + distilled water 70 mL.

Tensile tests were performed using a 1-tonne-class, small tensile tester (AGS-X; Shimadzu) of grip size about 22 mm. The welding test pieces were cut from the overall test pieces (25–50 mm in width and laser-welded for about 20 mm). Figure 4 presents a photograph of the tensile test system and the specimen specifications.

3. Experimental Results And Discussion

3.1 BOP characteristics of Al and Cu alloys

We varied the output and welding speeds of the laser core and ring beams to establish appropriate penetration conditions; we performed BOP experiments on separate Al and Cu plates to determine the beam energy absorption rates and thermal diffusions within the materials. The preliminary data that guided the simulations were acquired by observing the bead shape and cross-section of the Al surface by laser power and welding speed. As shown in Figure 5(a), the experiment was performed at welding speeds of 200~500 mm/s; the core and ring beam outputs ranged from 500~2,000 W.

BOP welding of the Al6061 alloy (thickness: 0.4 mm) revealed that welding conditions #1-1 to #2-1 were associated with high heat inputs causing excessive surface and backside beading, and melting. The optimal conditions for surface and back bead formation (complete penetration) were 700 W for the core beam, 500 W for the ring beam, and a welding speed of 200 mm/min which described as condition #3-2. The bead width ranged from 0.9–1.0 mm, and the computer simulation was based on these results.

Figure 5(b) presents the BOP welding conditions and macro-photographs revealing surface bead quality for the C1020P test material. Excessive discontinuity was evident early in welding of specimens #1-1, #1-2, and #2-1. To avoid this, we set the output slope to 1 mm to ensure that the laser beam did not interfere with keyhole welding of a substrate with a high reflectance and low beam absorption. For BOP welding of the C1020P alloy (thickness: 0.4 mm), the optimal conditions for formation of a sound surface and back beads (reflecting full penetration) were a core beam of 2.5 kW, a ring beam of 3 kW, and a welding speed of 200 mm/min.

The optimal conditions were thus those of #3-2 and #2-2, which eliminated discontinuity defects via output slope control early in welding. As shown in Figure 5, for the soft Al6061 specimen, a hole (a “piercing”) occurred early during welding, but a sound bead formed later when the output stabilized.

3.2 Lap joint welding of homogeneous Al-Al materials

Figure 6 presents the laser lap-welding results and cross-sectional views of homogeneous Al-Al materials. Welding proceeded by increasing the core beam output in 100-W steps from 800~1100 W, with adjustment of the ring beam output. As the laser power increased, so did the bead width and penetration depth; pores developed when partial penetration occurred at 800~1000 W. This likely reflects the fact that gas in the weld does not escape during high-speed aluminum welding. If full penetration is in play, gas is discharged from below even if pores are generated.

Figure 7 presents the bead widths and penetration depths for each position. To objectively compare the weld cross-sections, we investigated the relationships between the welding conditions and penetration depth (P_t), surface bead width (B_t), overlap joint bead width (B_m), and back bead width (B_b). Figure 7(a) defines the terminologies of geometry for the weld shapes and positions, and Figure 7(b) shows that when welding proceeded as the center beam output rose in 100-W steps, the width of the upper bead was not significantly affected, but the penetration depth increased. This did not significantly increase the upper bead width because the laser beam was initially largely reflected from the Al surface.

3.3 Surface and cross-sectional analysis of overlapping Al-Cu welds

Figure 8 presents the results of laser lap Al-Cu welding. The ring beam output (700 W), welding speed (200 mm/s), and focal position (± 0) were fixed; the center beam intensity was increased in 20-W steps from 820~900 W and the shapes of the welds were examined. As the output increased, the surface bead width (B_t) and the junction interface bead width (B_m) increased, attributable to the reflectivity of Cu. Even

when the center beam passed through the Al6061 test piece, the output did not affect penetration, given the low absorptivity of C1020P.

Brittle IMCs generated at Al-Cu interfaces or small pores in joint can impair weld strength. Figure 9 presents the widths of the Al-Cu laser junctions. The width of the interface between the surface bead and the joint tended to increase as the output increased, as also seen when Al was welded. Because the penetration was only partial, the back bead width and penetration depth were not available. Cross-sectional analysis revealed that the interface between C1020P and Al6160 was appropriate.

3.4 Tensile strengths of real welds and computer simulations

To explore the tensile strength by welding output, the core beam output was varied from 800 to 2000 W with the ring beam held at 700 W, the welding speed at 200 mm/s, and the focal position at ± 0 . Figure 10 presents the tensile test data on upper bead widths. The tensile strength was about 62 kg_f at 820 W, but did not increase thereafter when the welding power increased. However, the surface bead width increased as the welding power increased. After tensile testing, we found interfacial fractures of the Al-Cu interfaces in all specimens. We presume that these were brittle fractures, as suggested by the scatter diagram of tensile strength. In the 1500 and 2000 W tensile tests, most of the upper Al6061 welds fell onto the lower C1020P welds. Thus, the IMC thickness was excessive given the large heat input.

Computer simulation was conducted to estimate the heat distributions by the heat input ratios of the core and ring beams. We tested ratios of 1200/0 W, 0/1200 W, and 700/500 W for the core/ring beam power. As shown in Figure 11, when the total heat input was that of the core beam, the maximum temperature was 576°C; when the total heat input was that of the ring beam, the maximum temperature was 1360°C. However, experimentally, the maximum temperature was 860°C when the core/ring beam ratio was appropriate, thus allowing good temperature control.

Figure 12 presents the simulation results as the core/ring beam ratio varied. During simulation, the core and ring beams ranged from 0~1200 W but their sum was always 1200 W. Temperatures were calculated 0.5 mm distant from the center of the weld bead interface. In conclusion, we found that the ring beam output determined the size of the weld bead surface.

4. Conclusions

The characteristics of weld joint on the Al and Cu are studied for the separately controllable core and ring beams. The analysis was made for the individual BOP tests on Al and Cu, the homogeneous Al-Al materials and heterogeneous Al-Cu materials. The heat distributions were also analyzed via computer simulation. The conclusions are as follows:

(1) In terms of BOP welding of Al6061 and C1020P materials, the optimal conditions were a core beam of 700 W, a ring beam of 500 W, and a welding speed of 200 mm/s for Al6061. For C1020P, the optimal

conditions were a center beam of 2500 W, a ring beam of 3000 W, and a welding speed of 200 mm/s. Some initial welding defects could be eliminated via output slope control.

(2) On laser lap welding of Al-Al and Al-Cu, the bead width and the interfacial bead width at the junction increased when the output increased. The penetration depth did not vary markedly, but small pores formed at the interface of the junction.

(3) For homogeneous Al-Al materials, as the laser power increased, all of the upper bead width, joint interface bead width, and penetration depth tended to increase. However, welds associated with low heat inputs exhibited pores caused by partial penetration, but healthy welds without pores formed after full penetration.

(4) Tensile tests on the heterogeneous material revealed that the tensile strength did not increase as the welding power increased, remaining at about 60~70 kgf. The tensile strength fell to about 30~35 kgf at high energy inputs (1.5 and 2.0 kW) because of IMC formation at the interface of the weld; this heat input was excessive.

Declarations

5. Acknowledgement

This research was funded by the Korea Nation Research Foundation, grant no.: NRF-2019R1F1A1062594

The English in this document has been checked by at least two professional editors, both native speakers of English. For a certificate, please see: <http://www.textcheck.com/certificate/GNtbnj>

Affiliations – Department of Mechanical Engineering, Keimyung University, Daegu, 42601, South Korea

Data availability - The datasets generated during and/or analyzed during the current study are available from the corresponding author on reasonable request.

Statements and Declaration

The authors declare that they have no known competing financial interests or personal relationships that could have appeared to influence the work reported in this paper.

Funding - This work has been supported by the Korea Nation Research Foundation, grant no.: NRF-2019R1F1A1062594.

Conflict of interest - On behalf of all authors, the corresponding author states that there is no conflict of interest.

Ethical approval - Not applicable.

Consent to participate - Not applicable.

Consent to publish - Not applicable.

Author Contributions – HC: Conceptualization, Writing-review and editing, Experiment review, JC: Experiment, Formal analysis, Data curation, Writing—original draft preparation,; All authors have read and agreed to the published version of the manuscript.

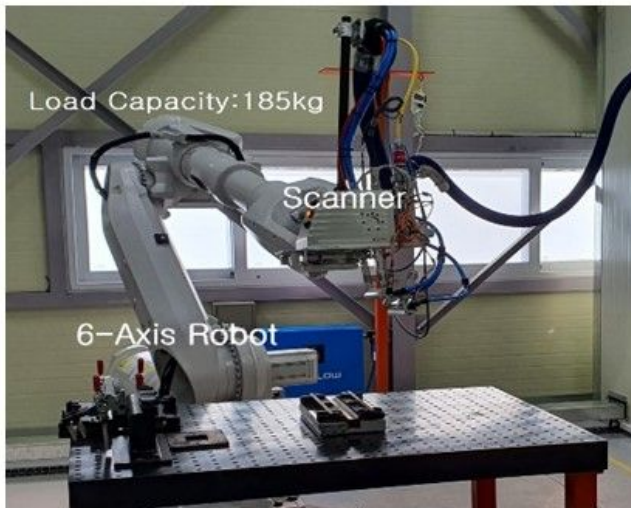
References

1. Mathivanan K, Plapper P (2019) Laser Welding of dissimilar copper and aluminum sheets by shaping the laser pulses. *Procedia manufacturing* 36:154–162. <https://doi.org/10.1016/j.promfg.2019.08.021>
2. Hung CH, Chen WT, Sehhat MH et al (2021) The effect of laser welding modes on mechanical properties and microstructure of 304L stainless steel parts fabricated by laser-foil-printing additive manufacturing. *Int J Adv Manuf Technol* 112:867–877. <https://doi.org/10.1007/s00170-020-06402-7>
3. Xu Y, Gong Y, Li P et al (2020) The effect of laser power on the microstructure and wear performance of IN718 superalloy fabricated by laser additive manufacturing. *Int J Adv Manuf Technol* 108:2245–2254. <https://doi.org/10.1007/s00170-020-05172-6>
4. Wang P, Chen X, Pan Q et al (2016) Capacity optimization in Industry Laser welding dissimilar materials of aluminum to steel: an overview. *Int J of Adv Manuf Technol* 98:9–12. <http://doi.org/10.1007/s00170-016-8725-y>
5. Punzel E, Hugger F, Dorringer R et al (2020) Comparison of different system technologies for continuous-wave laser beam welding of copper. *Procedia CIRP* 94:587–591. <http://doi.org/10.1016/j.procir.2020.09.081>
6. Kick M, Habedank J, Heilmeier J et al (2020) Contacting of 18650 lithium-ion batteries and copper bus bars using pulsed green laser radiation. *Procedia CIRP* 94:94:577–581. <http://doi.org/10.1016/j.procir.2020.09.079>
7. Schmalen P, Plapper P (2016) Evaluation of laser braze-welded dissimilar Al-Cu joints. *Physics Procedia* 83:506–514. <https://doi.org/10.1016/j.phpro.2016.08.052>
8. Hartel U, Ilin A, Bantel C, Gibmeier J et al (2016) Finite element modeling for the structural analysis of Al-Cu laser beam welding. *Physics Procedia* 83:1404–1414. <http://doi:10.1016/j.phpro.2016.08.147>
9. Garavaglia M, Demir A, Zarini S et al (2020) Fiber laser welding of AA 5754 in the double lap-joint configuration: process development, mechanical characterization and monitoring. *Int J of Adv Manuf Technol* 111:1643–1657. <http://doi.org/10.1007/s00170-020-06128-6>
10. Reisgen U, Olschok S, Jakobs S et al. Influence of the degree of dilution with laser beam vacuum-welded Cu-Al mixed joints on the electrical properties. *Procedia CIRP* 74; 2018; 74:23-26. <https://doi.org/10.1016/j.procir.2018.08.022>
11. Zhou X, Zhang G, Shi Y et al. Microstructures and mechanical behavior of aluminum-copper lap joints. *Materials Science & Engineering A*; 2017; 705;105–113.

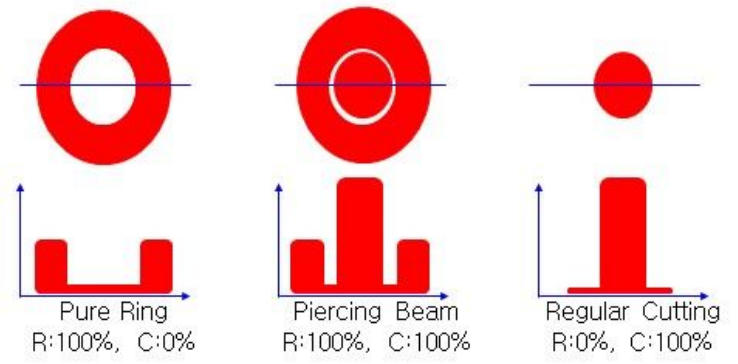
<https://doi.org/10.1016/j.msea.2017.08.056>

12. Brand M, Schmidt P, Zaeh M et al (2015) Welding techniques for battery cells and resulting electrical contact Resistances. *Journal of energy storage* 1:7–14. <http://doi:10.1016/j.est.2015.04.001>
13. Chen S, Zhai Z, Huang J et al (2015) Interface microstructure and fracture behavior of single/dual-beam laser welded steel-Al dissimilar joint produced with copper interlayer. *Int J of Adv Manuf Technol* 83:1–4. <http://doi:10.1007/s00170-015-7390-x>
14. Bono P. Laser welding of copper and aluminum battery interconnections, *Proceedings Industrial Laser Applications Symposium*; 2015; 9657. <http://doi.org/10.1117/12.2176048>
15. Kah P, Vimalraj C, Martikainen J et al (2015) Factors influencing Al-Cu weld properties by intermetallic compound formation. *Int J of Mechanical Materials Engineering* 10:1. <http://doi.org/10.1186/s40712-015-0037-8>
16. Coroado J, Meco1 S, Williams S et al (2017) Fundamental understanding of the interaction of continuous wave laser with aluminum. *Int J Adv Manuf Technol* 93:3165–3174. <http://doi.org/10.1007/s00170-017-0702-6>
17. Franciosa P, Serino A, Botros A (2019) R. et al. Closed-loop gap bridging control for remote laser welding of aluminum components based on first principle energy and mass balance. *Journal of Laser Applications* 31:022416. <http://doi.org/10.2351/1.5096099>
18. Hietala M, Hamada A, Keskitalo M et al. Mechanical characterization of laser-welded double-lap joints in ultra-high and low strength steels for sandwich panel applications. *Proceedings of materials today*; 2020; 28:455-460. <http://doi.org/10.1016/j.matpr.2019.10.031>
19. Elefante A, Nilsen M, Sikström F et al (2019) Detecting beam offsets in laser welding of closed-square-butt joints by wavelet analysis of an optical process signal. *Optics Laser Technology* 109:178–185. <https://doi.org/10.1016/j.optlastec.2018.08.006>
20. Kim T, Choi H (2021) Study on Laser Welding of Al-Cu Dissimilar Material by Green Laser and Weld Quality Evaluation by Deep Learning. *J of Welding Joining* 39:67–73. <http://doi.org/10.5781/JWJ.2021.39.1.8>
21. You H, Kang M, Yi S et al (2021) Modeling of Laser Welds Using Machine Learning Algorithm. *Journal of Welding Joining* 39:36–44. <http://doi.org/10.5781/JWJ.2021.39.1.4>

Figures



(a)



(b)

Fig. 1 Experimental setup (a) system (b) beam split schematic

Figure 1

See image above for figure legend.

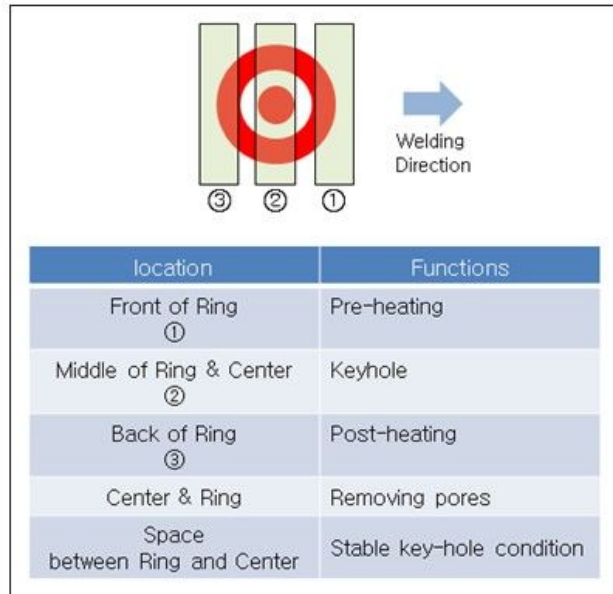
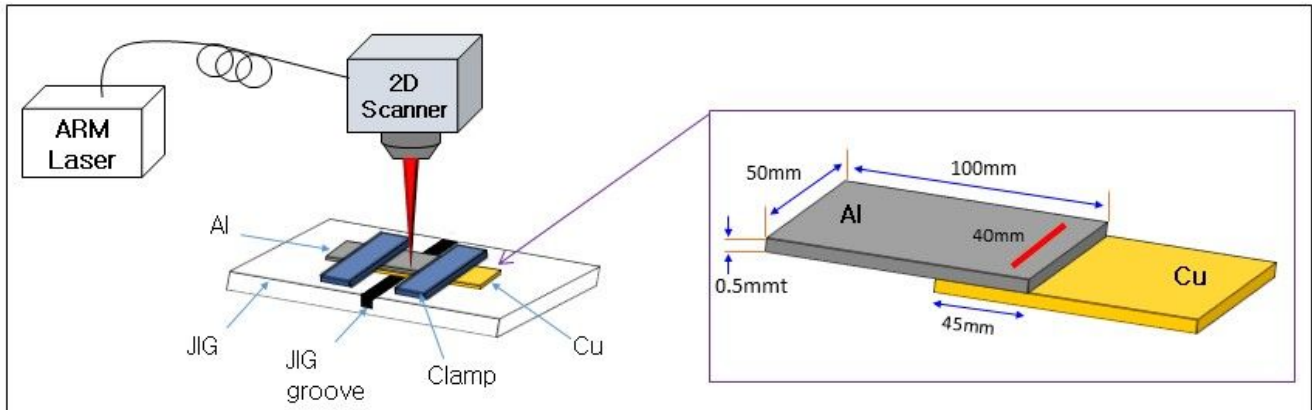
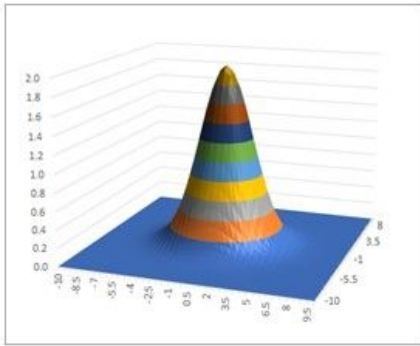


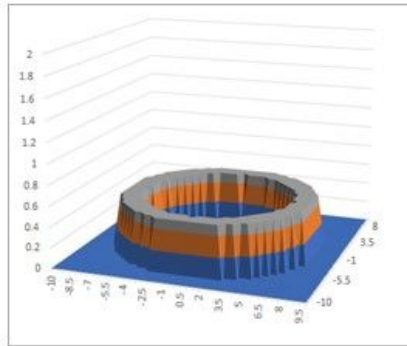
Fig. 2 Laser welding jig and heat input schematic

Figure 2

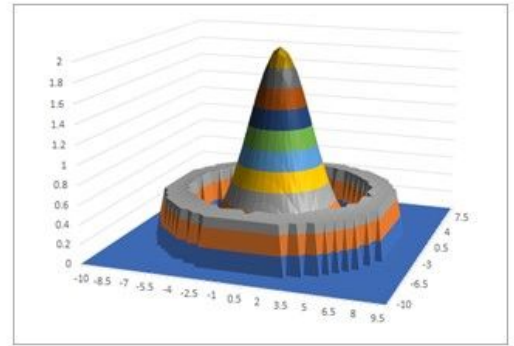
See image above for figure legend.



(a)



(b)



(c)

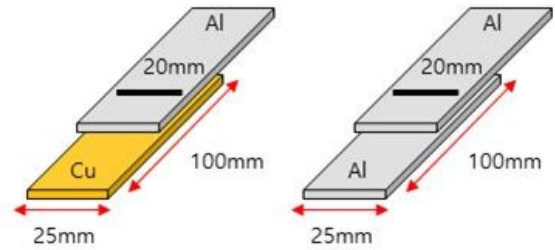
Fig. 3 Laser intensity distribution for (a) Gaussian core beam (b) Flat top ring beam (c) Combined beam

Figure 3

See image above for figure legend.



(a)



(b)

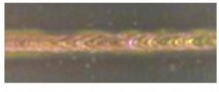
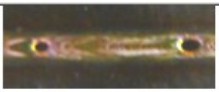
Fig. 4 Mechanical property test (a) tensile test machine (b) test specimen

Figure 4

See image above for figure legend.

Bead on Plate (liner welding)						
No.	Laser power(kW)		Speed (mm/sec)	Focus	Bead appearances	Remark
	Core beam	Ring beam				
1-1	1	2	500	±0		over weld
1-2	1	2	200			over weld
2-1	1	1	200			over weld
3-1	0.5	0.5	200			under weld
3-2	0.7	0.5	200			optimum (slope up)

(a)

Bead on Plate (liner welding)						
No.	Laser power(kW)		Speed (mm/sec)	Focus	Bead appearances	Remark
	Core beam	Ring beam				
1-1	3	2	200	±0		over weld
1-2	3	3	200			over weld
2-1	2.5	3	200			partially over weld
2-2	2.5	3	200			optimum (slope up)

(b)

Figure 5

BOP experiments for (a) aluminum and (b) copper material

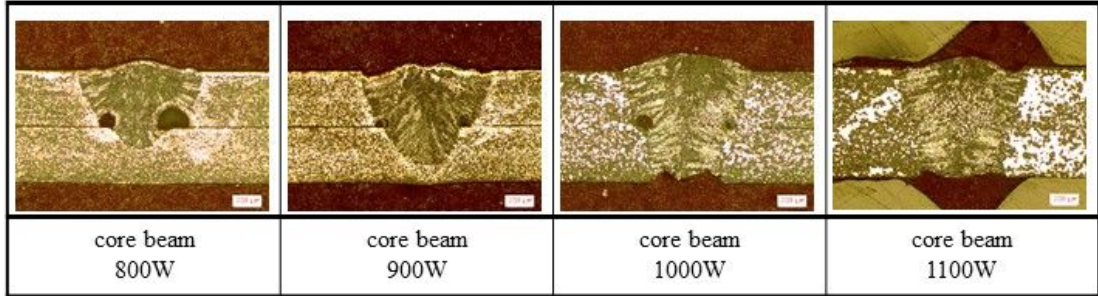


Fig. 6 Cross sectional view of Al-Al welding (ring beam 500W, speed 200mm/s)

Figure 6

See image above for figure legend.

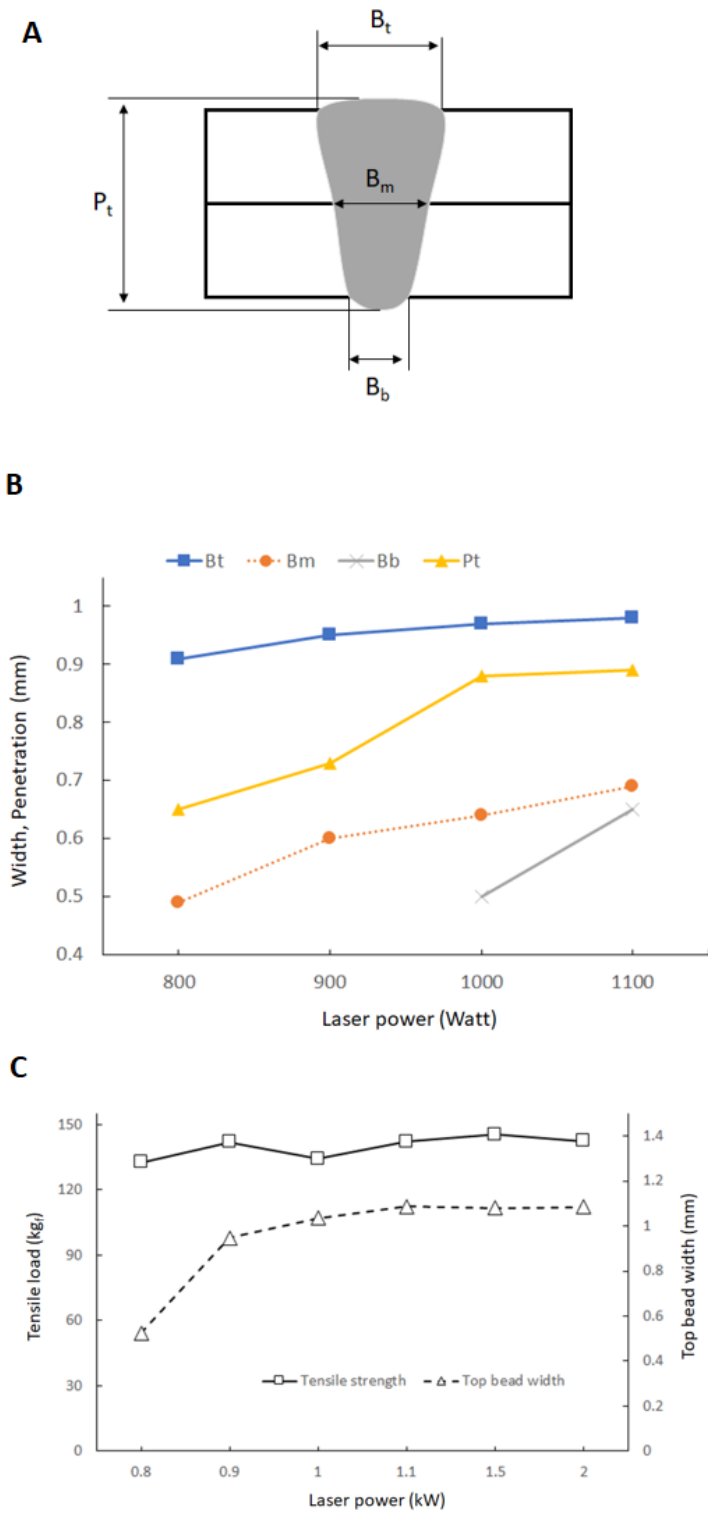


Figure 7

(a) Definition of weld geometry (b) Weld bead measurement per laser power (c) Tensile test results for aluminum-aluminum welding by various heat input

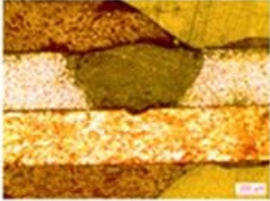
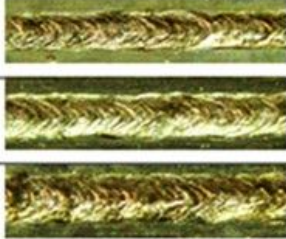
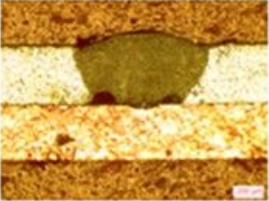
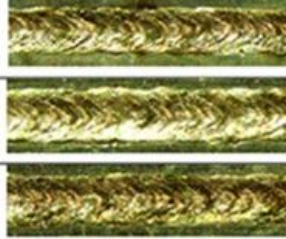
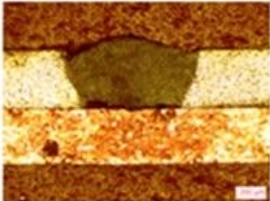
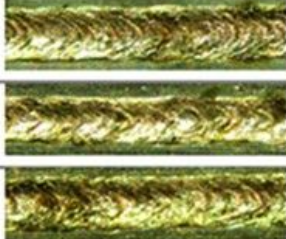
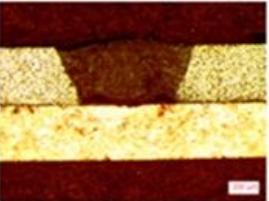
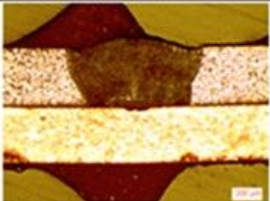
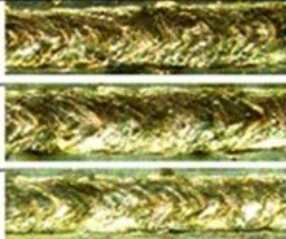
Welding conditions					
Ring beam: 700W, Speed: 200mm/s, Focus: ±0					
Weld section	Bead shape	Start	Weld section	Bead shape	Start
		Middle			Middle
		End			End
					
Center beam 820W		Center beam 840W			
					
Center beam 860W		Center beam 880W			
					
Center beam 900W					

Fig. 8 Cross sections of aluminum and copper welding

Figure 8

See image above for figure legend.

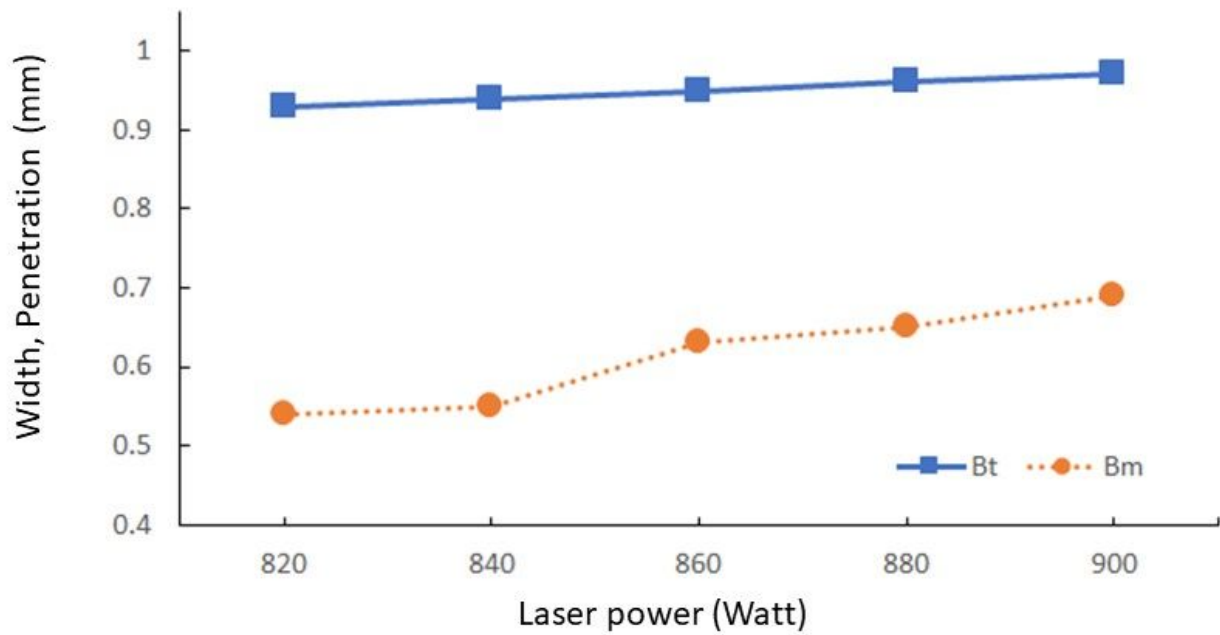


Fig. 9 Effect of laser power on bead formation for aluminum-copper welding

Figure 9

See image above for figure legend.

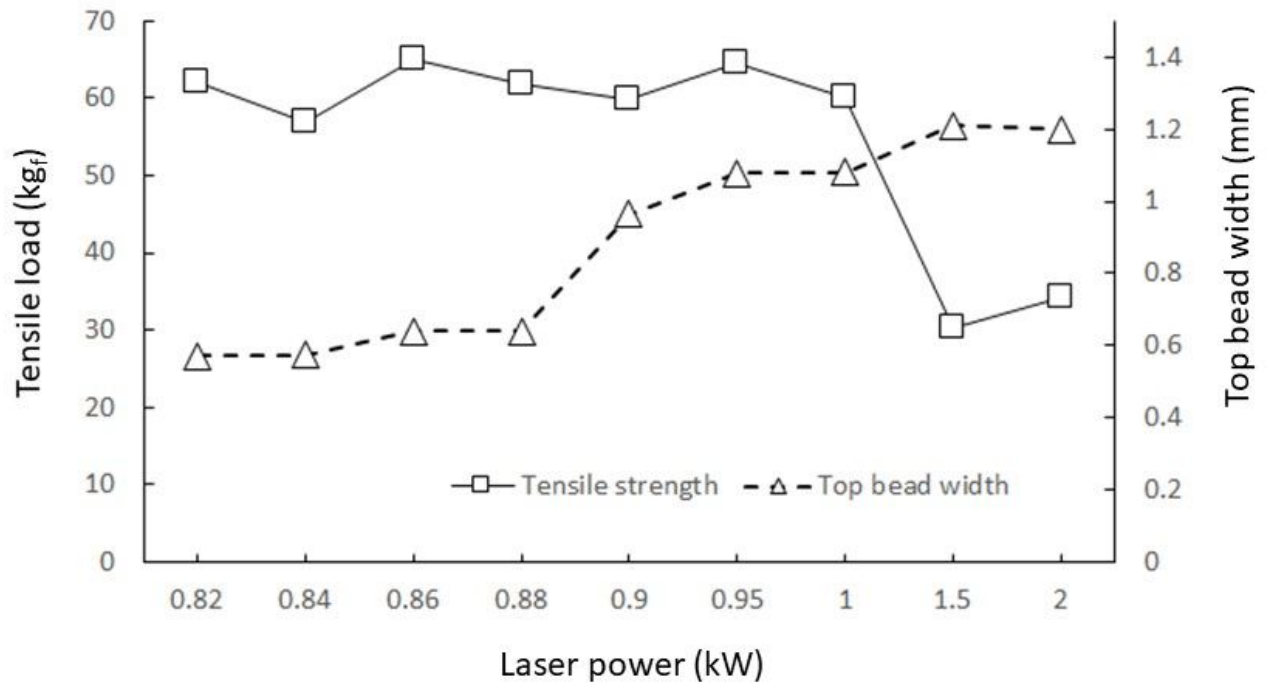


Fig. 10 Tensile test results for aluminum-copper welding by various heat input

Figure 10

See image above for figure legend.

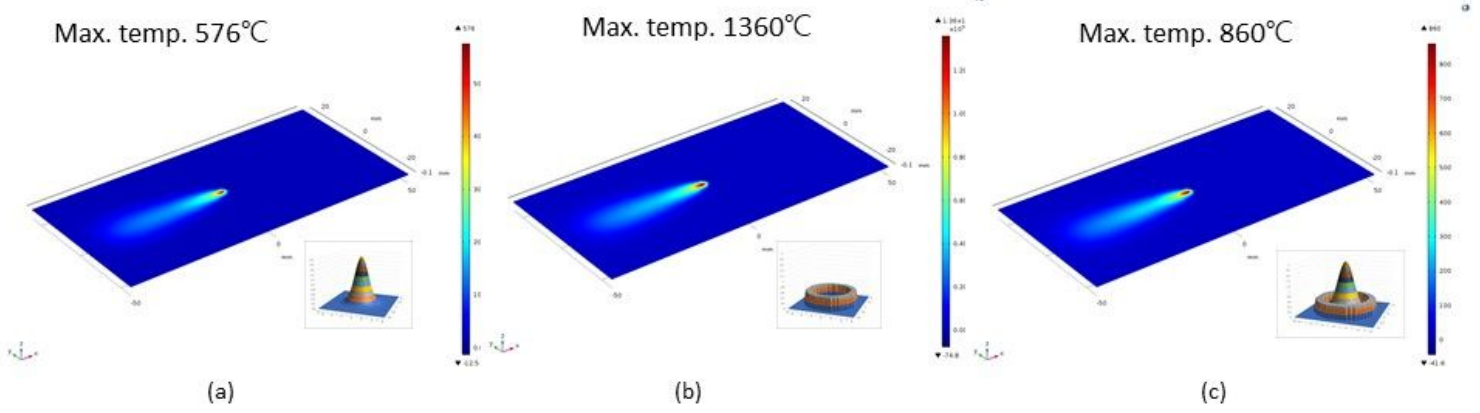


Fig. 11 Computer simulation for Core/Ring (a) 1200W/ 0W (b) 0W/1200W (c) 700W/500W

Figure 11

See image above for figure legend.

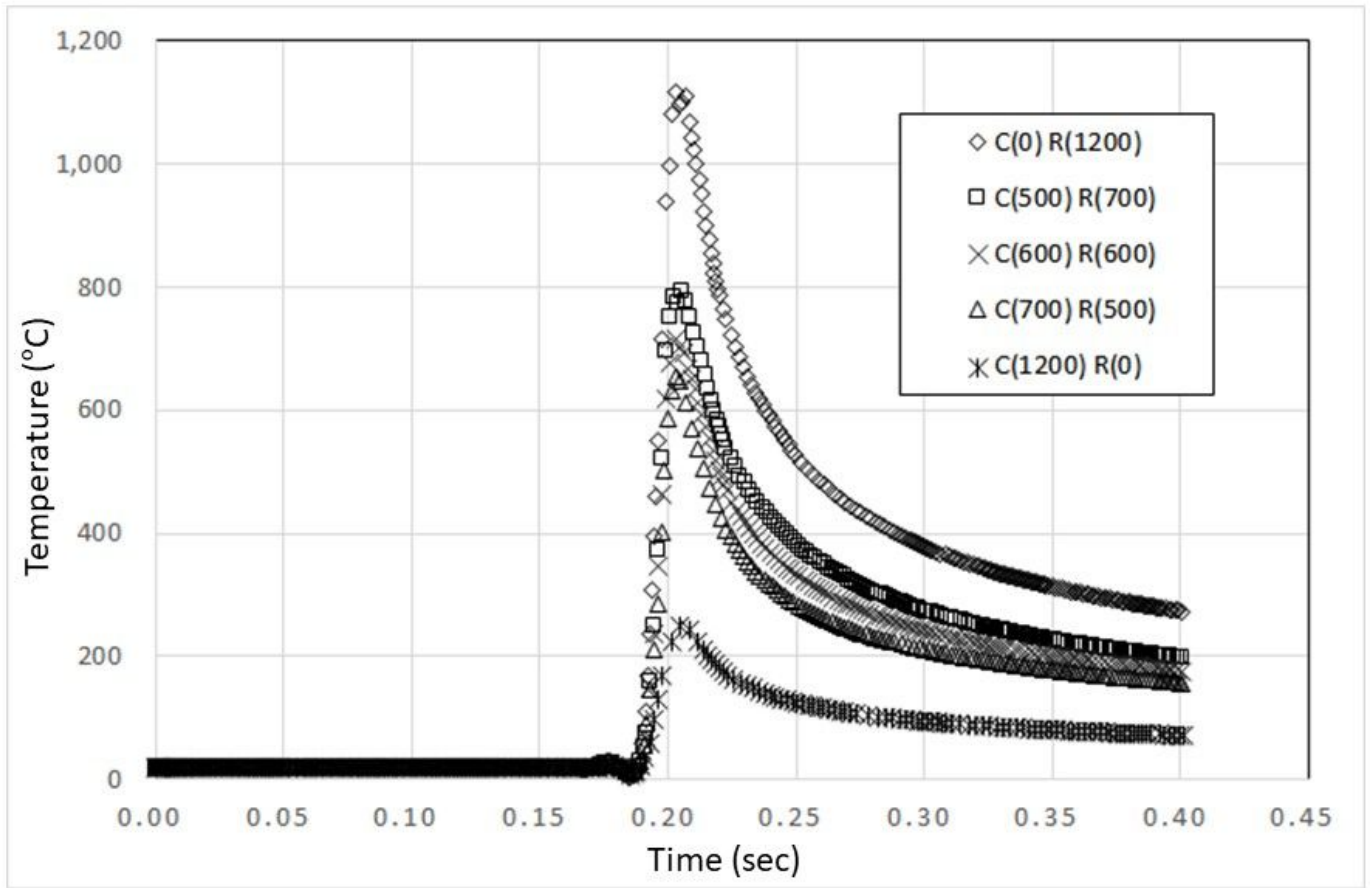


Fig. 12 Heat distribution for various heat input, C-core beam, R-ring beam

Figure 12

See image above for figure legend.